Available online at www.sciencedirect.com
ScienceDirect
Trans. Nonferrous Met. Soc. China 35(2025) 3414−3427
Transactions of Nonferrous Metals Society of China
www.tnmsc.cn

Enhanced strength−ductility synergy of ultrafine-grained eutectic−dendrite complex structures in zirconium/nickel electron beam welded joints

Xin-yan TENG[1], Guo-qing CHEN[1], Ge ZHANG[1], Yang XIANG[2], Xue-song LENG[3]

1. State Key Laboratory of Advanced Welding and Joining, Harbin Institute of Technology, Harbin 150001, China;
2. Beijing Shiny Tech. Co., Ltd., Beijing 100048, China;
3. Institute of Special Environments Physical Sciences, Harbin Institute of Technology (Shenzhen), Shenzhen 518055, China

Received 22 February 2024; accepted 15 November 2024

Abstract: Insufficient metallurgical compatibility between Zr and Ni can lead to the formation of brittle welds and introduce thermal stress-related challenges during the electron beam welding process. Through the implementation of beam deflection and vibration, a transformation was achieved in the primary Ni_5Zr dendrite structure, transitioning from a mass into a layered configuration, consequently resulting in the formation of an ultrafine-grained eutectic−dendrite complex structure. It is revealed that the enhanced strength−ductility synergy of this structure significantly contributes to the high tensile strength and improved plasticity observed in the welded joints. As a result, the welding cracks are effectively mitigated, and notable advancements are achieved in the mechanical properties of Zr/Ni joints, elevating the tensile strength of the joints from 36.4 to 189 MPa. This research not only highlights the potential of this technique in enhancing the strength and ductility of Zr/Ni welded joints but also serves as a valuable reference for future investigations involving welding applications of dissimilar metals.

Key words: electron beam welding; composite structure; strength−ductility synergy; mechanical properties

1 Introduction

The increasing global focus on nuclear power development in response to environmental and energy challenges has highlighted the importance of zirconium/nickel (Zr/Ni) joints. Given the large safety factors, the attainment of high strength and high ductility in materials is arguably a vital requirement for the nuclear industry [1]. Zirconium serves as a widely employed material for fuel cladding, while nickel is recognized as a cost-effective and high-strength structural material within the nuclear industry. The application of zirconium−nickel components aids the cost-effectiveness, making zirconium/nickel electron beam welded joints an important technological target [2,3].

Zirconium alloys are sensitive to welding impurities, as small amounts of N, C, O, and other elements in tungsten inert gas (TIG) welding can lead to decreased corrosion resistance and high-temperature oxidation resistance. The properties in the heat-affected zone (HAZ) also tend to deteriorate [4]. Zirconium exhibits excellent weldability on its own. ZENG et al [5] achieved joint strength comparable to the base metal in Zr705 diffusion bonding at 960 °C. Diffusion bonding of zirconium with dissimilar alloys such as stainless steel is challenging and often requires the use of metal interlayers such as Ti, Cu, and Al to inhibit metallurgical reactions [6]. To braze Zr and SiC, LUO et al [7] prepared a CoCrFeNiCuSn interlayer, wherein the joint matrix consists of a

Corresponding author: Guo-qing CHEN, Tel: +86-18945063917, E-mail: chenguoqing@hit.edu.cn
https://doi.org/10.1016/S1003-6326(25)66889-0

solid solution phase due to the high-entropy effect, improving the joint's strength and thermal stability. Between the welding temperature intervals, zirconium and nickel exhibit a high degree of mutual insolubility [8]. Poor metallurgical compatibility can result in a non-homogeneous interface and brittle weld [9]. Differences in expansion coefficients typically cause high thermal stress during the process, resulting in residual stress, part deformation, and crack generation [10,11].

Given these challenges, it is very difficult to obtain a high-quality Ni/Zr joint using the traditional fusion welding method. Electron beam welding possesses high energy density, fast heating and cooling speeds, narrow welding seam, and small heat-affected zone [12]. In this study, heat input and conditions were optimized by beam deflection and vibration during the welding process. The original primary Ni_5Zr dendrite inherent in weld changed from a massive structure to a layered structure. The as-obtained weld with ultrafine-grained eutectic−dendrite complex structures possessed high tensile strength with relatively high plasticity. A full investigation has been performed on the formation mechanism and characteristics of the complex structure.

2 Experimental

2.1 Experimental materials and welding method

The pure zirconium (R60702) and nickel (N6) used as base materials for welding were produced by Taiyuan Iron and Steel Co., Ltd. in China. Their chemical compositions and mechanical properties are given in Table 1−3. The performance of the base materials differed significantly, as shown in Table 3. Before the welding process, the working surface of the R60702 tubes and N6 rods was polished using sandpaper ranging from 400 to 1500 grit sequentially to remove the oxide film, degreased with alcohol, and subsequently quickly blown dry.

The microstructure of the base metal is shown in Fig. 1. The as-rolled R60702 tube has a typical textured grain along the axial direction. The cold rolled and annealed N6 rod possesses single-phase fcc austenite morphology with a twin structure, elongated along the axial direction.

2.2 Welding equipment and process parameters

The welding process was carried out in a MEDARD45 device (Techmeta, France) at an accelerating voltage of 55 kV. As shown in Table 4, the welding parameter was optimized by scanning and deflection. The optimized welding parameter promoted molten pool flow and reduced melting ratio by scanning and deflection. The assembled specimen was clamped by a rotatable three-jaw chuck inside a vacuum chamber. The electron gun remained immobile and the electron beam was focused on the surface during the welding process, as shown in Fig. 2.

2.3 Characterization of joint

The welded specimens were processed by wire-cut electrical discharge machining (WEDM) to obtain metallographic specimens, transmission specimens, and tensile test specimens. The metallographic specimens mounted in resin were burnished with sandpaper from 240# to 7000# and

Table 1 Composition of pure nickel (N6) (wt.%)

Ni	Mg	C	S	P	Cu	Fe	Si	Mn	Zn
99.6	0.08	0.01	0.005	0.002	0.008	0.007	0.08	0.05	0.007

Table 2 Composition of pure zirconium (R60702) (wt.%)

Hf	Fe	Cr	C	N	O	H	Zr
2.24	0.06	0.01	0.007	0.004	0.069	0.0007	Bal.

Table 3 Physical properties of Zr and Ni

Material	Melting point, T_m/°C	Linear expansion coefficient, $\alpha/10^{-6}$ K^{-1}	Thermal conductivity, λ/(W·m^{-1}·K^{-1})	Tensile strength, σ_b/MPa	Specific heat capacity/(J·kg^{-1}·K^{-1})
R60702	1855	6.42	370	620	668
N6	1455	13	71.4	443	444

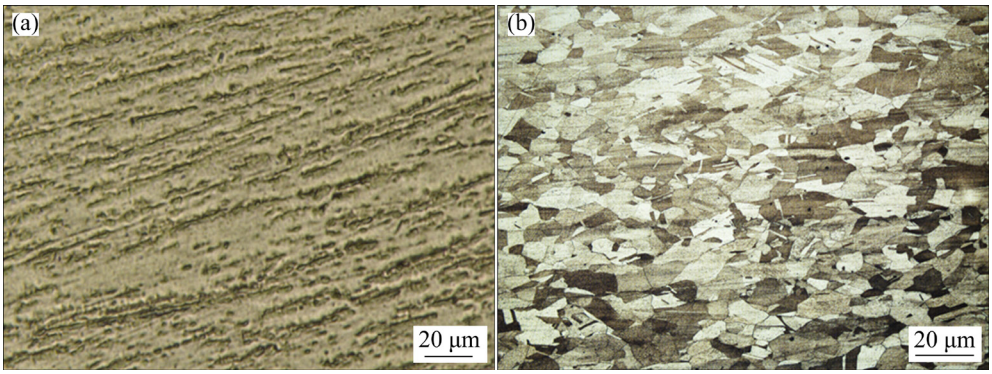

Fig. 1 Microstructures of base metal: (a) R60702; (b) N6

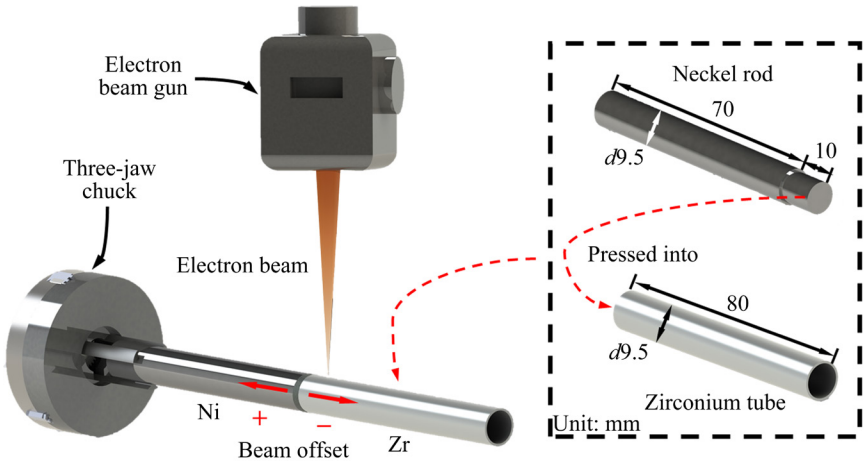

Fig. 2 Schematic diagram of assembly steps

Table 4 Detailed welding parameters

Welding method	Accelerating voltage/kV	Welding speed/(mm·min^{-1})	Beam offset/mm	Welding current/mA	Vibration amplitude/mm
Direct welding			0		
Deflection to Ni	55	240	0.5	6	2
Deflection to Zr			−0.3		

polished using 2.5 μm diamond paste, and then were etched for 15 s with a solution consisting of 100 mL distilled water, 20 mL hydrochloric acid, and 5 g $CuSO_4$, followed by ultrasonically cleaning with acetone. Then, ultrathin transmission specimens (50 μm) prepared by WEDM and sandpaper were ion-milled using a Gatan PIPSTM until the small hole at the center of the sample was made.

2.4 Mechanical properties testing of joint

Optical micrographs were acquired on a Keyence VHX−1000 microscope with polarized light. A Zeiss Merlin Compact scanning electron microscope was used to characterize the morphology of the weld and tensile fracture, and electron dispersive spectroscopy (EDS) mode was applied for elemental analysis. The morphological characterization was performed by FEI Tecnai G2 F30 transmission electron microscopy. Phase compositions were obtained using X'Pert-PRO X-ray diffraction (XRD) implementing.

Tensile tests were carried out using an Instron−5569 material testing machine under an initial strain rate of 1×10^{-3} s^{-1}. The tensile specimen dimension was determined according to GB6397—86 standard [13]. To fasten with uniform force, a metal cylinder was plugged into the tube, as shown in Fig. 3. The microhardness of the joints was tested on the HXD−1000TM microhardness instrument with a load of 200 g and a dwell time of 15 s. To better reflect the hardness distributions, 60 test points

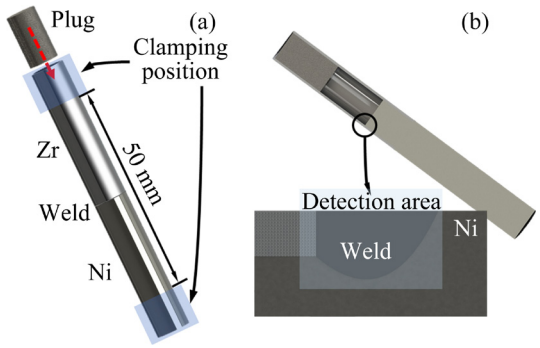

Fig. 3 Schematic view of specimen preparation for tests: (a) Clamping; (b) Sampling position

were arranged in 6 rows, and 10 columns were selected to completely cover the joint. Subsequently, an intuitive hardness distribution cloud map was created by importing the obtained hardness data into the Origin for plotting.

3 Results and discussion

3.1 Weld formation

The direct welding joint exhibited a smooth and flat surface, achieving leak rates below 9.0×10^{-8} Pa·m^3/s during helium measurement, which met airtightness requirements. The cross-sectional morphology of the joint is depicted in Figs. 4(a, b). Under electron beam vibration, the weld seam displayed a bowl-like shape, with a depth of 0.71 mm and a width of 1.74 mm. The internal structure of the weld seam was uniform, characterized by an overall basket-weave morphology and stratified solidification features. The welding thermal cycle induced severe thermal stress at the contact surface, given thermal expansion coefficient of zirconium being only half that of nickel. Consequently, the intermetallic compound (IMC) layer at the bottom became the initial crack formation point under stress, leading to numerous microscopic cracks occurring in the IMC layer, and macroscopic cracks extending into the weld. The heat dissipation direction at the edge of the weld seam is consistent, and the heat dissipation rate is faster, resulting in smaller orientation differences and larger areas for each block at the edge. As the primary Ni_5Zr phase is formed, the Zr concentration decreases to the eutectic region, and

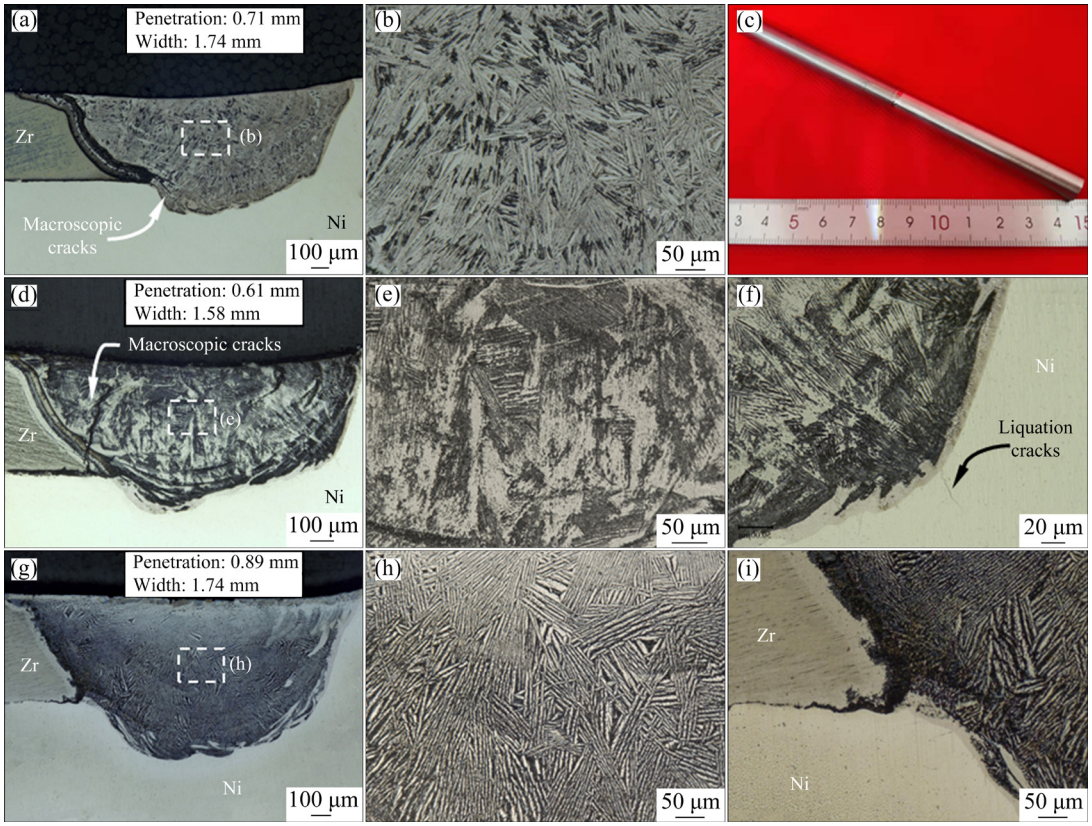

Fig. 4 Macroscopic cross sectional morphology (a), microstructure (b) and specimen after welding (c) in direct welding; Macroscopic cross sectional morphology (d), microstructure (e) and liquation cracks (f) in deflection to Zr; Macroscopic cross sectional morphology (g), microstructure (h) and weld toe (i) in deflection to Ni

the temperature drops to approximately 1170 °C. At this point, the (γ-Ni+Ni_5Zr) eutectic phase is formed in the interdendritic spaces. During this process, the primary Ni_5Zr phase competes with the eutectic phase for growth, and undercooling significantly impacts the morphology of Ni_5Zr [14].

According to the Ni−Zr phase diagram shown in Fig. 5, the two elements produce only intermetallic compounds during solidification due to their low mutual solubility (<3%). The molten pool undergoes a eutectic reaction in multiple temperature and concentration intervals: γ-Ni+Ni_5Zr generation at 1170 °C, $Ni_{21}Zr_8$+$Ni_{10}Zr_7$ generation at 1070 °C, $Ni_{21}Zr_8$+$Ni_{10}Zr_7$ generation at 1010 °C, and $NiZr_2$+β-Zr generation at 960 °C. Preliminary experiments indicated that the weld was built with coarse Ni/Ni_5Zr dendrites and (Ni+Ni_5Zr) eutectic structure. Controlling the morphology of eutectics is crucial for enhancing performance. Enhanced strength−ductility synergy in ultrafine-grained eutectic−dendrite holds the most promising potential. WU et al [15] developed a heterogeneous structure of bimodal grains in titanium that contain 30% soft, coarse-grained lamellae embedded in an ultrafine-grained matrix. By creating large strain gradients across the lamella interfaces during deformation, the resulting materials exhibited remarkable ductility. In these structures, soft lamellae are almost as strong as the hard matrix due to the full deformation constraint imposed by the hard lamella matrix [16]. Inspired by the studies above, a remarkable strength−ductility enhancement is expected if we can obtain a similar structure. In order to further optimize joint performance, research on beam offset welding was conducted.

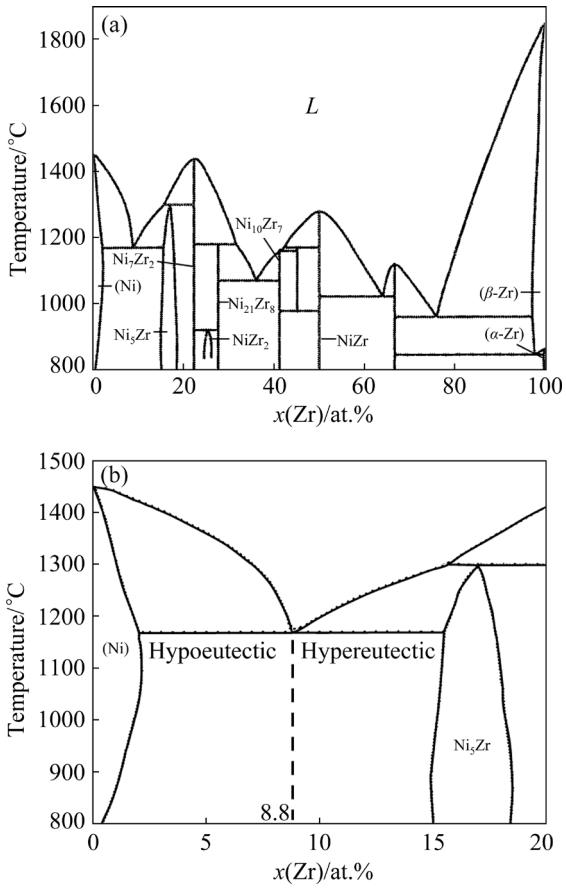

Fig. 5 Complete phase diagram (a) and local phase diagram (b) of Ni−Zr binary system

When the beam was deflected towards Zr, the joint depth and width decreased significantly, as shown in Fig. 4(d). Figures 4(e, f) show that precipitated Ni_5Zr phase transformed from a basket-weave structure to a coarser structure and became the main component of the weld seam, increasing weld joint brittleness, with cracks extending into the weld seam center, causing joint failure at the initial stage of tensile testing.

To refine the morphology of the Ni_5Zr primary phase and reduce its proportion, offset Ni welding was performed. After optimization, deflecting towards Ni by 0.5 mm successfully eliminated cracks in the joint, as illustrated in Figs. 4(g, h). Observations showed that under the same heat input, the depth and width of the weld seam increased, and the proportion of nickel in the seam further increased. The weld seam structure exhibited a basket-weave pattern with layered solidification characteristics. The amount of Ni_5Zr primary phase in the seam decreased, and the morphology became more uniform. The thickness of the brittle reaction layer was reduced. Near the fusion line on the nickel side, strip-like phases precipitated, primarily due to the high viscosity in the liquid state and the small temperature range between the solid and liquid phase lines of nickel. Under rapid cooling, these phases accumulated at the edge of the weld seam, where they reacted and solidified to form strip-like phases mainly composed of primary γ-Ni and eutectic structures. Due to the increased heat input on the nickel side, liquation cracks were formed at the fusion line and extended into the heat-affected zone, where they were filled with eutectic liquid phase, as shown in Fig. 4(i).

Nickel and nickel alloys tended to form liquation cracks during welding, as shown in Fig. 4(f) [17]. During the rapid heating and cooling

process of welding, Zr elements or other impurity elements in the supersaturated solid solution at high temperatures segregated at grain boundaries, forming liquid films and carbides, or the residual eutectic melted, forming the liquid film directly that reduced the interfacial bonding strength, and the lattice distortion caused by the element segregation at the grain boundary also reduced the bonding strength between adjacent grains, resulting in crack initiation and propagation. Welding line energy and welding speed directly determine the thickness of the intergranular liquid film, which significantly impacts the sensitivity of the liquation cracks in the heat-affected zone of nickel and nickel-based alloys, as given in Eq. (1):

$$\sigma=2\gamma_{sl}/h \quad (1)$$

where σ represents the critical tensile stress, γ_{sl} represents the solid−liquid surface tension, and h represents the thickness of the liquid film. Therefore, as the liquid film thickness decreases, the tensile stress increases, heightening the tendency for crack formation. The liquid phase penetrates and fills the cracks through capillary action, and the diffusion process consumes some of the liquid phase. Simultaneously, under continuous high welding heat input conditions, the heat-affected zone remains at high temperatures for a period. The liquid can solidify again, repairing the cracks in their initial stage.

3.2 Microstructures of joints

Figure 6 presents a comparison of the XRD patterns for the weld, where the types of phases in the welds remain essentially unchanged under different welding conditions, with the diffraction peaks of γ-Ni and Ni_5Zr being the most prominent. The diffraction peak of Ni_5Zr is significantly enhanced in the weld deflected towards Zr, indicating an increase in the Ni_5Zr phase content. Moreover, the diffraction peak of $NiZr_2$ also starts to appear while the diffraction peak of γ-Ni is enhanced in deflection to Ni joint, suggesting the presence of the $NiZr_2$ phase in the reaction layer.

According to the Ni−Zr binary phase diagram, the weld composition generates primary Ni_5Zr phase when the Zr content is less than 20% and is located in the hypereutectic region. And primary γ-Ni phase is generated when the weld composition is located in the hypoeutectic region. Then, ultrafine (γ-Ni+Ni_5Zr) eutectic structure is generated in the interstitial space of the primary phases. Figure 7(a) displays the position located at the bottom of the zirconium-side reaction layer, where the three regions correspond to the hypoeutectic, eutectic, and hypereutectic concentration intervals.

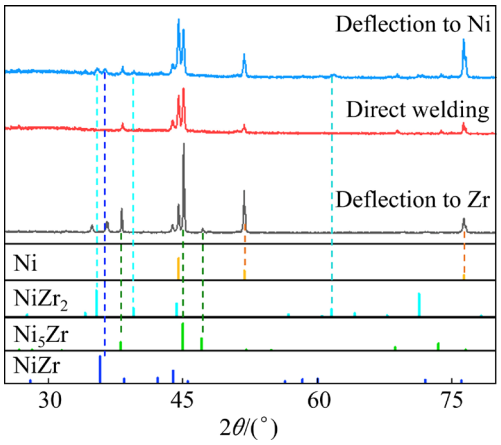

Fig. 6 XRD patterns of weld with different welding methods

Due to the difference in atomic radii, Zr hardly diffuses into the Ni-base material [18]. The microstructure at the edge of the weld seam grows preferentially along the direction of the fastest heat dissipation, i.e., from the edge of the weld seam vertically towards the center. Due to the rapid heat dissipation at the edge of the weld seam, significant element segregation occurs, resulting in a coarse microstructure primarily concentrated near the fusion line on the zirconium side, as shown in Fig. 8(a). In contrast, the center of the weld seam has a uniform element distribution and slower heat dissipation, presenting a fine lamellar structure.

The content of Zr element further decreases in the weld, leading to a reduction in the formed Ni_5Zr phase. Ni_5Zr tends to grow without orientation, consistent with the dendrite-like morphology observed in the weld seam [14]. Environmental conditions can also influence the morphology of Ni_5Zr. At the edge of the weld, the heat dissipation rate is faster. Under high cooling rates and large undercooling, atomic diffusion is insufficient, resulting in a clearer interface of Ni_5Zr dendrites. At the bottom of the weld seam, the fusion line exhibits an irregular hook-like morphology, mainly due to the weakened electron beam stirring effect, causing non-uniform mixing phenomena, as shown in Fig. 8(d).

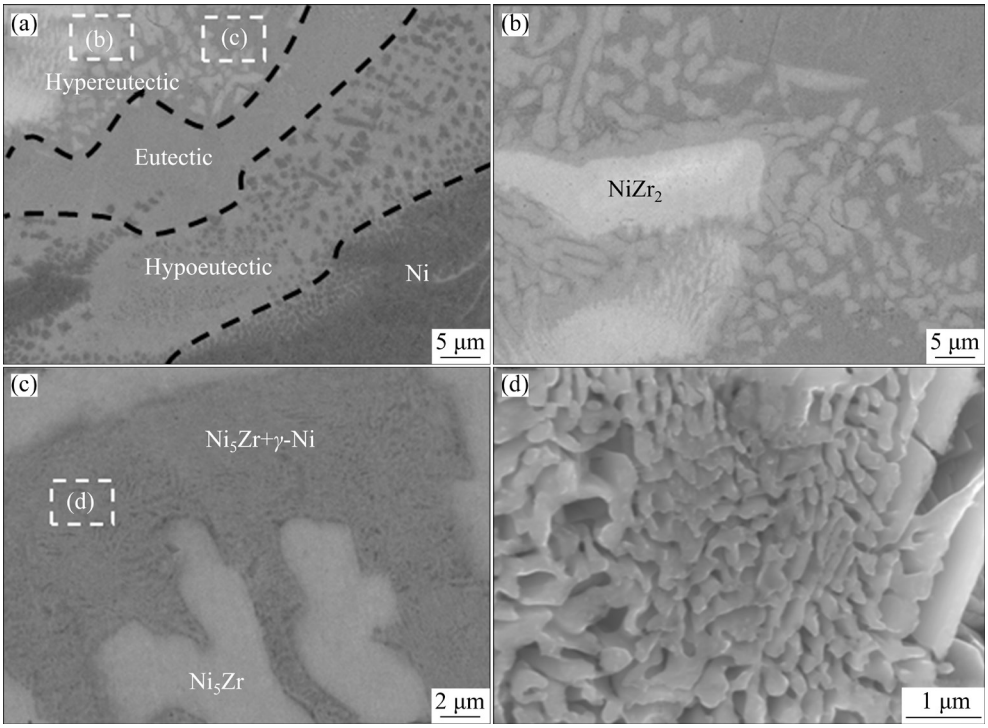

Fig. 7 SEM images of weld at fusion line (a) and hypoeutectic region (b); Eutectic microstructure (c) and magnified eutectic microstructure (d)

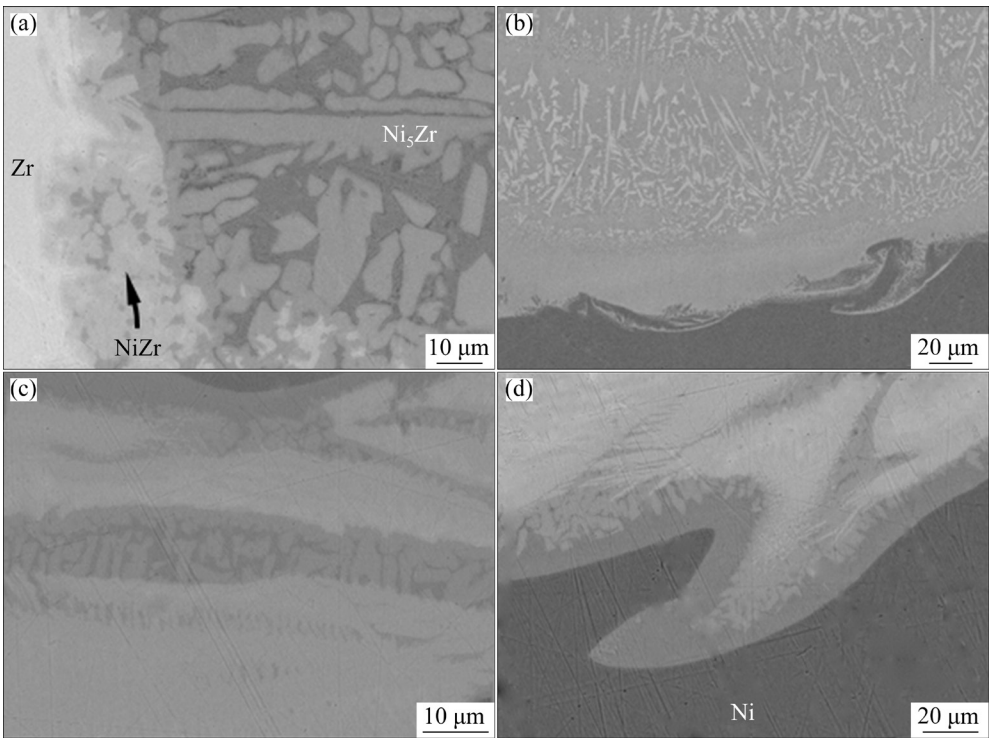

Fig. 8 Fusion line of beam offset to Ni: (a) On Zr side; (b) On Ni side; (c) At edge; (d) At bottom

The fine (γ-Ni+Ni_5Zr) eutectic structure was analyzed using high-angle annular dark-field scanning transmission electron microscopy (HAADF-STEM), as shown in Fig. 9, with the morphologies that are spherical, lamellar, or "tadpole" shaped. The "tadpole" morphology features a spherical head and a lamellar tail, representing an intermediate mode between the

spherical and lamellar morphologies. The formation mechanism of irregular eutectics is currently under debate, and the theories proposed for this formation are specific to particular alloy systems [19,20].

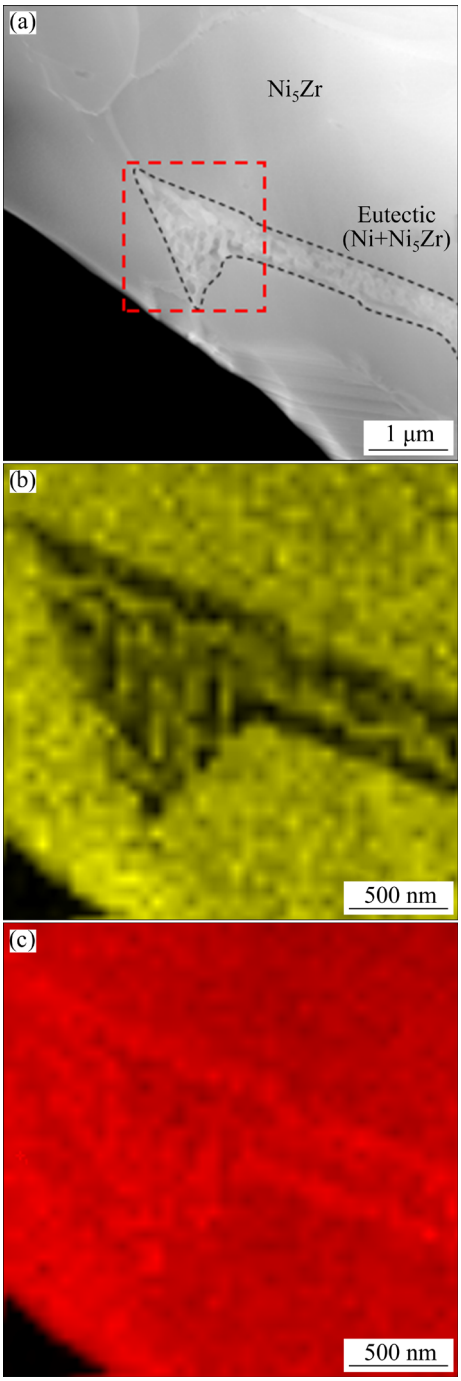

Fig. 9 HAADF-STEM image and EDX elemental maps: (a) Morphology of eutectic; (b) Distribution of Zr; (c) Distribution of Ni

The internal morphology of the weld seam is shown in Fig. 10. Based on the phase diagram, the interior of the weld seam consists of elongated Ni_5Zr and eutectic (γ-Ni+Ni_5Zr) phases occupying the interstices. In the initial stage, the large driving force generated by the Gibbs free energy difference between the undercooled melt pool liquid and the primary Ni_5Zr phase causes rapid growth of the primary Ni_5Zr phase, while the driving force for the subsequent eutectic reaction is smaller and the transformation rate is slower. Due to latent heat release, the interface between the eutectic phase and dendrites becomes blurred, the morphology of the dendrites is disrupted, and some dendritic fragments are formed. At the top of the weld seam, the smaller number and larger spacing of primary Ni_5Zr result in a higher degree of elongated dendrite fragmentation. This ultrafine eutectics−dendrite composite structure, composed of micron-scale primary phases with secondary dendrites and ultrafine eutectic matrix phases, undergoes plastic deformation mainly through the shear slip mechanism. The constraining effect of the brittle−hard dendrites makes shear slip difficult, while the dislocation and multiplication of shear bands effectively release and accommodate accumulated shear strain, endowing the structure with high strength and plastic deformation capability, which is beneficial for the performance of the joint.

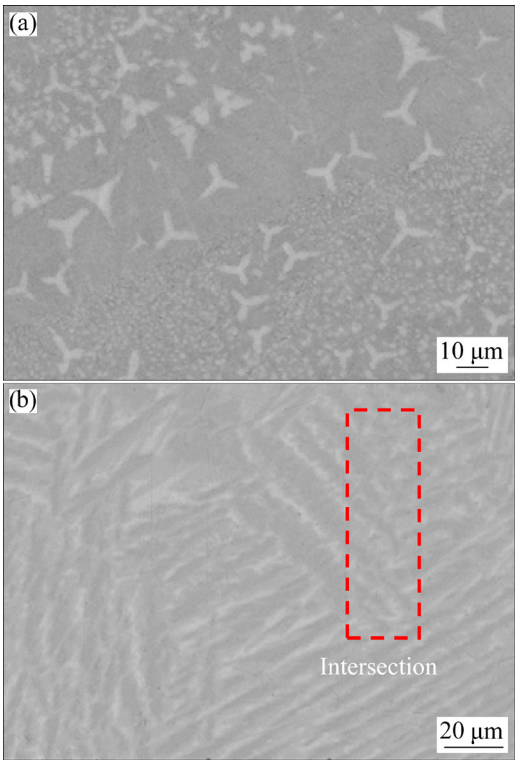

Fig. 10 SEM images in middle of weld (a) and at edge of weld (b)

Influenced by cooling rate and elemental distribution, primary Ni_5Zr exhibits varying orientation arrangements in different regions, growing in the same direction within a single region and resulting in Ni_5Zr structures with diverse sizes and directions of block distribution. When the growth of grain in a block is hindered by the grain in another block, the preferentially growing grain obstructs the growth of subsequent grains, causing some grains at the intersections of different orientations to fracture. The fractured grains, affected by the latent heat of crystallization, melt again and solidify attached to already grown grains, forming polygonal structures or even smaller grains, and subsequently ceasing expansion at the boundaries.

Based on these observations, it is hypothesized that the anomalous eutectic formation mechanism occurs under large undercooling conditions, with Ni_5Zr in the eutectic growing as dendritic or lamellar structures. Then, with the involvement of residual liquid or under solid-state conditions, local remelting or decomposition occurs, forming irregular eutectics through secondary solidification.

3.3 Solidification process of weld

Initially, nickel has a relatively large diffusion coefficient in zirconium [18]. Vacancy defects on the zirconium surface create local chemical potential gradients. At high temperatures, surface diffusion occurs to reduce these gradients, forming a body-centered cubic structure of β-Zr solid-solution containing Ni elements at the edge of the molten pool. During the rapid cooling process of electron beam welding, the faster cooling rate is sufficient to suppress the transformation of β-Zr to α-Zr, potentially leaving some β-Zr solid solution at the edge of the molten pool.

The composition of the molten pool near the fusion line is mainly Zr, suggesting that β-Zr precipitates first in the molten pool, followed by a rapid decrease in Zr concentration. When the temperature drops to around 960 °C, the first eutectic reaction occurs, precipitating $NiZr_2$+β-Zr. According to the lever rule, the amount of precipitated $NiZr_2$ is much greater than that of β-Zr. β-Zr preferentially grows on the previously precipitated β-Zr with consistent crystal structure, and $NiZr_2$ begins to precipitate from the super-saturated β-Zr as well. However, some β-Zr does not undergo rapid solidification, resulting in the formation of supersaturated β-Zr deposited on the $NiZr_2$ matrix, which appears in SEM images as a supersaturated solid solution with a similar contrast to the zirconium matrix.

In regions slightly farther from the fusion line, eutectic liquid phases (NiZr+$NiZr_2$) are also formed at a very close temperature of 1010 °C. According to the lever rule, the precipitation amount of NiZr is smaller, and it precipitates at the edge of the reaction layer. During this process, brittle phases such as β-Zr, NiZr, and $NiZr_2$ continuously precipitate, ultimately disrupting the continuity with the matrix and resulting in the formation of a relatively thick continuous IMC phase at the zirconium-side fusion line. In the middle weld joint, the morphology of the zirconium fusion line is similar in all locations, with multilayer reaction products formed by the above reactions.

The weld is mainly composed of the initially precipitated Ni_5Zr and the subsequently precipitated eutectics. As the beam deflects to Ni, the proportion of Zr elements in the weld decreases, the number of primary Ni_5Zr decreases, and the morphology transforms into a triangular shape. The distinct layer-by-layer solidification phenomenon is observed in the weld. The structure at the center of the weld is composed of large triangular Ni_5Zr and the eutectics of (γ-Ni+Ni_5Zr) filling in between, while the adjacent layer is solely composed of triangular Ni_5Zr and γ-Ni.

At the bottom of the weld, the electron beam stirring effect is weakened, resulting in uneven mixing of the molten pool and a large concentration gradient, with NiZr or $NiZr_2$ intermetallic compounds present. During cooling, a large number of primary γ-Ni phases nucleate and grow in the sub-eutectic region at the edge of the molten pool. When the temperature drops below the eutectic transition temperature (T_E), the remaining liquid phase transforms into (γ-Ni+Ni_5Zr) eutectics, eventually forming a transition region composed of γ-Ni and eutectic structure between the nickel matrix and the weld. Near the Zr side, due to the higher Zr concentration, the primary phase is Ni_5Zr, and then the remaining liquid phase solidifies into (γ-Ni+Ni_5Zr) eutectics. This area is eventually composed of bar or polygonal Ni_5Zr and eutectic structure filling in between, with a large number of primary crystals, small spacing, and fewer eutectics,

which is conducive to the production of divorced eutectics. Therefore, the interface between the primary Ni_5Zr phase and the eutectic structure is relatively blurred, and due to the large thermal undercooling, the (γ-Ni+Ni_5Zr) eutectic structure becomes finer.

The liquid phase in the over-eutectic concentration range produces various morphologies of primary Ni_5Zr on the zirconium side. The cooling rate has a significant impact on the growth of Ni_5Zr, and as the cooling rate increases, the dendrites of primary Ni_5Zr become more developed. The liquid phase concentration gradient at the dendrite front changes, further promoting the nucleation and growth of the eutectic structure. Since Ni_5Zr itself does not have a preferred orientation for growth, but the heat dissipation rate is the fastest perpendicular to the welding interface, the large primary Ni_5Zr dendrites appear near the fusion line, growing preferentially in a direction perpendicular to the welding interface.

3.4 Characteristics of ultrafine-grained eutectics−dendrite complex structures

Experiments have demonstrated that the growth of anomalous eutectics is very complex, and the commonly accepted model based on partial remelting of primary phases cannot provide a perfect explanation [21]. Phase-field simulation has determined that anomalous eutectics preferentially occur at the center of the molten pool with high-temperature gradients and low cooling rates [22].

To explain the ease of eutectic formation in the Zr−Ni binary system, the relationship between the distribution coefficient (k_e) and the proportion of the residual molten pool liquid (f_L) can be discussed [23]. In non-equilibrium solidification processes such as electron beam welding, the effective distribution coefficient (k_e) is represented by Eq. (2):

$$k_e=\frac{k_0}{k_0+(1-k_0)\exp(-v\delta/D_L)} \tag{2}$$

where k_0 is the equilibrium partition coefficient; v is the solidification rate of the weld pool; δ is the thickness of the reaction layer at the weld pool boundary; D_L is the diffusion coefficient.

The radius of Zr atoms reaches 155 pm, while that of Ni atoms is 135 pm [24]. The diffusion resistance of Zr elements in the Ni lattice is relatively large, which intensifies the segregation in the eutectic reaction layer near the fusion line, making it difficult to diffuse into the Ni parent material. When the larger Zr atomic radius hinders diffusion, the diffusion coefficient (D_L) decreases, and the equilibrium partition coefficient (k_e) increases, as can be seen from Eq. (2).

The relationship between the remaining liquid composition in the weld pool and k_e can be described by Eq. (3):

$$f_L=\sqrt[k_e-1]{c_E/c_0} \tag{3}$$

where c_E is the concentration of the eutectic liquid; c_0 is the initial concentration of the weld pool.

In the above equation, c_E and c_0 can be considered as fixed constants. Therefore, as the partition coefficient (k_e) of the weld pool increases, a larger proportion of the weld pool concentration reaches c_E, facilitating eutectic formation. In conclusion, the large atomic radius of zirconium is an important reason for the formation of a substantial amount of eutectics in the weld seam.

The transmission electron microscopy bright-field image of the NiZr eutectics and the Ni dendrite in the weld is shown in Fig. 11. Due to its brittleness and hardness, the Ni_5Zr in the weld is difficult to deform. However, Ni, with its low stacking fault energy, produces a large number of twin lamellae in the dendrite [25]. The dislocations at the phase interface of Ni in the eutectics are distorted, forming a network of dislocations. Both Ni structures exhibit strong plasticity, and Ni and Ni_5Zr together form enhanced strength−ductility synergy, which improves the mechanical properties of the weld and suppresses crack propagation [26].

3.5 Mechanical properties

As shown in Fig. 12, comparative observations indicate that the weld hardness is generally higher than that of the base material with various welding parameters, and the hardness inside the weld has a large fluctuation. The high hardness area is mainly concentrated near the Zr fusion line, with a hardness value reaching HV 600. With different welding parameters, due to the differences in the quantity and distribution of brittle Ni_5Zr phases, the size of the high hardness area differs. In the Zr-biased welding method, a large number of Ni_5Zr phases are generated, and most of the weld shows

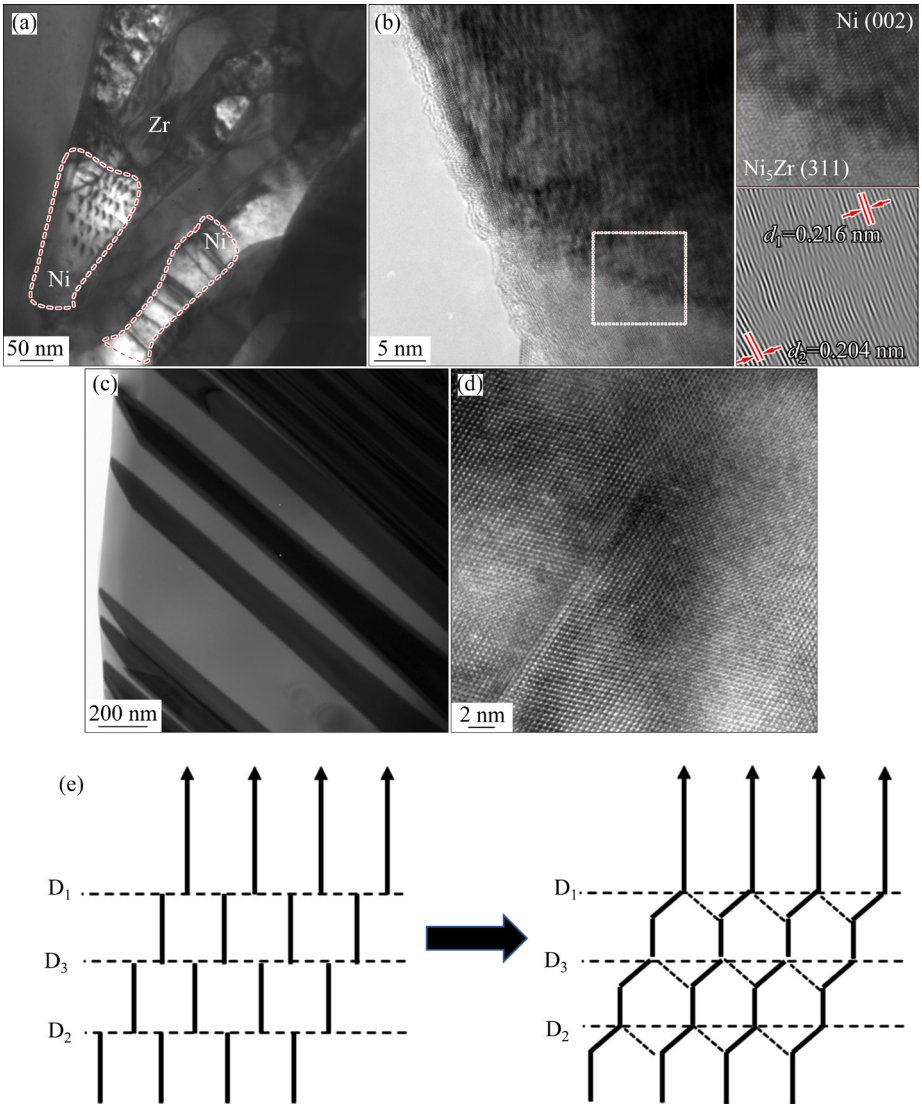

Fig. 11 Bright field (a) and high resolution (b) TEM images of eutectics; Bright field (c) and high resolution (d) TEM images of twin; Schematic illustration of dislocation network formation (e)

high hardness area, consistent with the results of microstructure observation. In the Ni-biased welding method, the amount of brittle Ni_5Zr phase is small. High hardness is localized near the Zr fusion line, while the rest of the weld maintains a hardness of around HV 300. Therefore, deflection welding effectively reduces the weld brittleness and improves joint strength from 36.4 to 189 MPa.

Upon examining the secondary electron image of the fracture surface of the joint, it is found that due to the high aspect ratio of the weld seam, the fracture locations differ across various regions of the joint. Therefore, it is not straightforward to determine the fracture location of the welded joint with different parameters. As depicted in Fig. 13, this region represents a transitional area in the fracture location. The fracture position is situated near the fusion line on the zirconium side. It is conjectured that the crack initiation occurs on the continuous NiZr and $NiZr_2$ IMC layers, which exhibit inferior mechanical properties. Subsequently, the crack extends towards the proximate Zr heat-affected zone and the interior of the weld seam. In the transitional zone, eutectic structures adhering to the fracture surface can also be observed, with a minor portion of the fracture surface presenting distinct cleavage steps. The β-Zr near the fusion line possesses a body-centered cubic structure, exhibiting noticeable river patterns and cleavage steps on the fracture surface. Furthermore, some fracture surfaces are located within the weld seam, and display a parallel lamellar structure with well-defined edges. All of the fractures above are characteristics of a typical brittle cleavage fracture.

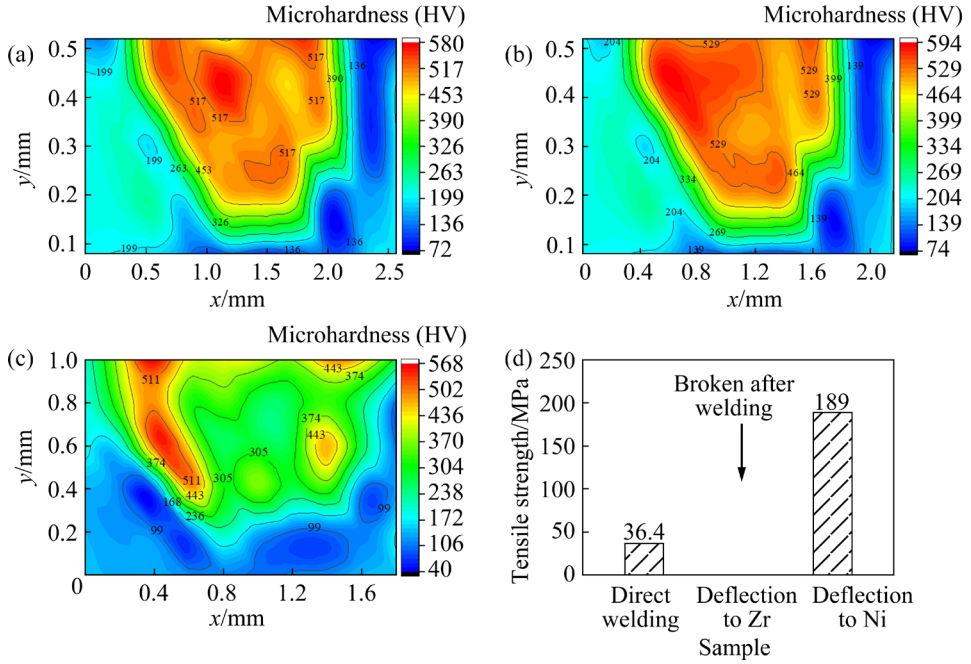

Fig. 12 Hardness distributions of direct welding (a), deflection to Ni (b), and deflection to Zr (c); Tensile test results (d)

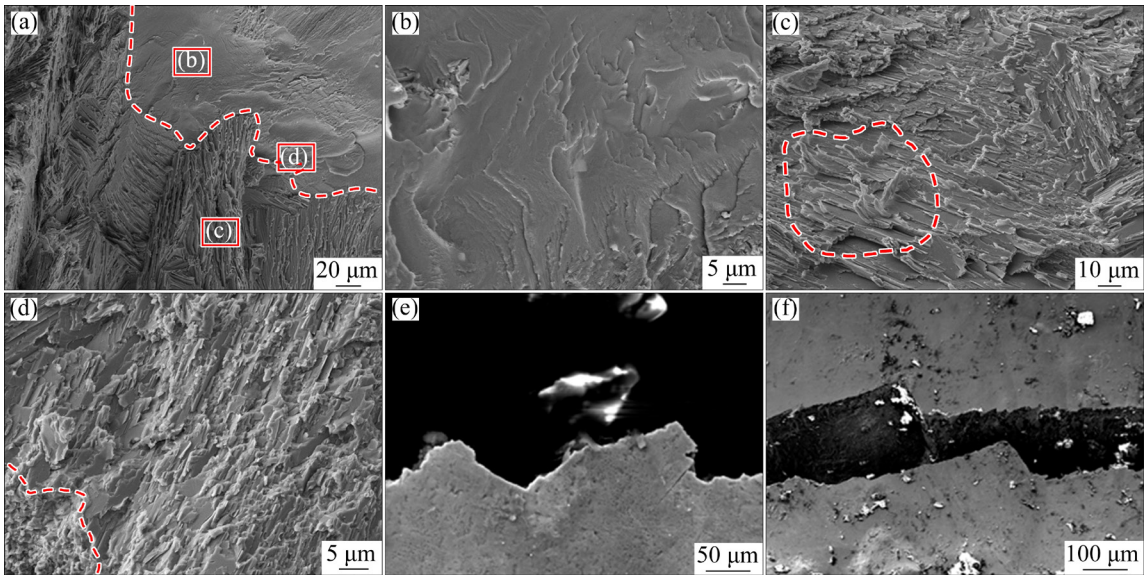

Fig. 13 Fractographies of overall topography (a), at Zr side (b), in weld (c), and in transition zone (d); Macroscopic morphologies of fracture (e, f)

4 Conclusions

(1) In symmetrical welding, the joint is formed well, and the weld seam exhibits a shallow, narrow bowl-shaped morphology. However, welding cracks are generated at the bottom lock position. The microstructure consists of a composite structure of primary Ni_5Zr/γ-Ni with secondary dendrites and (Ni_5Zr+γ-Ni) eutectics. The structure gradually refines towards the center from the periphery, and the difference in atomic radius is the main reason for promoting the formation of eutectics. Due to the hardness on zirconium side exceeding HV 600 and the generation of cracks near the continuous reaction layer, brittle fracture occurs near the reaction layer during tensile testing, and the tensile strength of the joint is 36.4 MPa.

(2) In beam offset welding, the proportion of Ni_5Zr precipitated in the weld seam gradually decreases, and the microstructure further refines. The formed ultrafine eutectics−dendritic structure

has better strength and plastic deformation ability due to the strong plasticity synergistic effect. Finally, the cracks at the bottom lock position disappear, the maximum hardness of the joint decreases to HV 540, the tensile strength reaches 189 MPa, and the joint performance is improved compared to symmetrical welding.

(3) Due to its brittleness and hardness, the Ni_5Zr in the weld is difficult to deform. However, Ni, with its low stacking fault energy, produces a large number of twin lamellae in the dendrite. The dislocations at the phase interface of Ni in the eutectics are distorted, forming a dislocation network. Both Ni structures exhibit large plasticity. Together, Ni and Ni_5Zr introduce an enhanced strength−ductility synergy, improving mechanical properties of the weld.

CRediT authorship contribution statement

Xin-yan TENG: Writing − Original draft; **Guo-qing CHEN:** Project administration; **Ge ZHANG**: Writing − Review & editing; **Yang XIANG:** Investigation; **Xue-song LENG:** Supervision.

Declaration of competing interest

The authors declare that they have no known competing financial interests or personal relationships that could have appeared to influence the work reported in this paper.

Acknowledgments

This work was supported by the National Natural Science Foundation of China (No. 52375322).

References

[1] ZHOU Si-yu, MA Guang-yi, WU Dong-jiang, CHAI Dong-sheng, LEI Ming-kai. Ultrasonic vibration assisted laser welding of nickel-based alloy and Austenite stainless steel [J]. Journal of Manufacturing Processes, 2018, 31: 759−767.

[2] SLOBODYAN M S. Resistance, electron- and laser-beam welding of zirconium alloys for nuclear applications: A review [J]. Nuclear Engineering and Technology, 2021, 53: 1049−1078.

[3] ZENG Ming, WANG Shi-cheng, DUAN Jin-hui, SUN Jing-hui, ZHONG Peng-yuan, ZHANG Ying-jie. Review of nuclear power development in China: Environment analysis, historical stages, development status, problems and countermeasures [J]. Renewable and Sustainable Energy Reviews, 2016, 59: 1369−1383.

[4] SLOBODYAN M S. Arc welding of zirconium and its alloys: A review [J]. Progress in Nuclear Energy, 2021, 133: 103630.

[5] ZENG Sheng, YOU Guo-qiang, YAO Fan-jin, LUO Jing-chuan, TONG Xin. Effect of bonding temperature on the microstructure and mechanical properties of the diffusion-bonded joints of Zr705 alloy [J]. Materials Science and Engineering A, 2021, 804: 140782.

[6] ZHANG Z, LI J, LIU K, WANG J, JIAN S J, XU C, WANG H, WANG L X, ZHU X L, OKULOV A, WEI Y D, YANG Y. Diffusion bonding, brazing and resistance welding of zirconium alloys: a review [J]. Journal of Materials Research and Technology, 2023, 26: 395−416.

[7] LUO Zhen-yuan, WANG Gang, ZHAO Yu, TAN Cai-wang, HE Ru-jie. Brazing SiC ceramics and Zr with CoCrFeNiCuSn high entropy alloy [J]. Ceramics International, 2022, 48: 23325−23333.

[8] MIURA M, OGAWA K. Welding and bonding of zirconium and its alloys [J]. Welding International, 1989, 3: 591−596.

[9] LI Yu-long, LIU Yan-ru,YANG Jin. First principle calculations and mechanical properties of the intermetallic compounds in a laser welded steel/aluminum joint [J]. Optics & Laser Technology, 2020, 122: 105875.

[10] ZHOU Jie, GUO Shun, DUAN Meng-wei, PENG Yong, GU Jie-ren, ZHOU Qi, WANG Ke-hong. Microstructure and mechanical properties of vacuum electron beam welded joints of Ti/Cu dissimilar metals [J]. Vacuum, 2023, 216: 112451.

[11] GUO Shun, PENG Yong, CUI Chong, ZHOU Qi, XU Jun-qiang, ZHU Jun. Forming and tensile fracture characteristics of Ti−6Al−4V and T2 Cu vacuum electron beam welded joints [J]. Vacuum, 2019, 165: 311−319.

[12] LI Yan-jun, WU Ai-ping, LI Quan, ZHAO Yue, ZHU Rui-can, WANG Guo-qing. Effects of welding parameters on weld shape and residual stresses in electron beam welded Ti2AlNb alloy joints [J]. Transactions of Nonferrous Metals Society of China, 2019, 29: 67−76.

[13] LIAO Heng-cheng, XU He-ting, HU Yi-yun. Effect of RE addition on solidification process and high-temperature strength of Al−12%Si−4%Cu−1.6%Mn heat-resistant alloy [J]. Transactions of Nonferrous Metals Society of China, 2019, 29: 1117−1126.

[14] WANG H P, LÜ P, CAI X, ZHAI B, ZHAO J F, WEI B. Rapid solidification kinetics and mechanical property characteristics of Ni−Zr eutectic alloys processed under electromagnetic levitation state [J]. Materials Science and Engineering A, 2020, 772: 138660.

[15] WU Hua-duo, HAN Yuan-fei, LE Jian-wen, ZONG Nan, LI Shao-peng, LUO Yi-fei, HUANG Guang-fa, MAO Jian-wei, LU Wei-jie. Enhanced strength-ductility synergy in fiber-like structural titanium matrix composites by controlling TiB content [J]. Journal of Alloys and Compounds, 2022, 915: 165399.

[16] WU Di, HAO Meng-yuan, ZHANG Tian-long, WANG Zhen, WANG Jiang, RAO Guang-hui, ZHANG Li-gang, DING Chao-yi, ZHOU Ke-chao, LIU Li-bin, WANG Dong, WANG Yun-zhi. Heterostructures enhance simultaneously strength and ductility of a commercial titanium alloy [J]. Acta Materialia, 2023, 257: 119182.

[17] CHEN Z, TAHERI M. The effect of pre-heating and pre-cold treatment on the formation of liquation and solidification cracks of nickel-based superalloy welded by laser beam [J].

Journal of Materials Research and Technology, 2020, 9: 11162−11177.
[18] ALLISON H W, SAMELSON H. Diffusion of aluminum, magnesium, silicon, and zirconium in nickel [J]. Journal of Applied Physics, 1959, 30: 1419−1424.
[19] STEFANESCU D M, ALONSO G, LARRAÑAGA P, SUAREZ R. On the stable eutectic solidification of iron−carbon−silicon alloys [J]. Acta Materialia, 2016, 103: 103−114.
[20] ZHAI Shuo-yan, LIU Jun-cheng, LIU Qiang. Microstructure evolution and toughening mechanism of Al_2O_3/YSZ directionally solidified eutectic ceramic [J]. Journal of Alloys and Compounds, 2021, 873: 159760.
[21] MULLIS A M, CLOPET C R. On the origin of anomalous eutectic growth from undercooled melts: Why re-melting is not a plausible explanation? [J]. Acta Materialia, 2018, 145: 186−195.
[22] LEI Wei, CAO Yong-qing, LIN Xin, CHANG Kun, HUANG Wei-dong. Globular to lamellar transition during anomalous eutectic growth [J]. Modelling Simul Mater Sci Eng, 2020, 28: 065014.
[23] LIU Li-feng, LI Jin-fu, ZHOU Yao-he. Solidification of undercooled eutectic alloys containing a third element [J]. Acta Materialia, 2009, 57: 1536−1545.
[24] TENDLER R, ABRIATA J P. Atomic size and fast diffusion of metallic impurities in zirconium [J]. Journal of Nuclear Materials, 1987, 150: 251−258.
[25] DING Qing-qing, LI Su-zhi, CHEN Long-Qing, HAN Xiao-dong, ZHANG Ze, YU Qian, LI Ji-xue. Re segregation at interfacial dislocation network in a nickel-based superalloy [J]. Acta Materialia, 2018, 154: 137−146.
[26] SHI P J, REN W L, ZHENG T X, REN Z M, HOU X L, PENG J C, HU P F, GAO Y F, ZHONG Y B, LIAW P K. Enhanced strength–ductility synergy in ultrafine-grained eutectic high-entropy alloys by inheriting microstructural lamellae [J]. Nat Commun, 2019, 10: 489.

锆/镍电子束焊接接头中超细共晶−枝晶复合结构的强韧性协同强化

滕新颜[1]，陈国庆[1]，张 戈[1]，向 阳[2]，冷雪松[3]

1. 哈尔滨工业大学 先进焊接与连接国家重点实验室，哈尔滨 150001；
2. 北京航天新立科技有限公司，北京 100048；
3. 哈尔滨工业大学(深圳) 特殊环境物质科学研究院，深圳 518055

摘 要：锆和镍之间的冶金相容性差，导致焊缝脆性高，在电子束焊接过程中热应力影响下产生焊缝开裂。通过电子束扫描及偏束焊接，实现焊缝中初生 Ni_5Zr 树枝晶形貌从块状向片层状转变，形成超细共晶−枝晶复合结构。该结构具有的优异强韧性协同效应显著提高焊接接头的抗拉强度和塑性。结果表明，焊缝中裂纹得到有效抑制，锆/镍接头的力学性能显著提升，抗拉强度从 36.4 MPa 提高到 189 MPa。此研究不仅在提升锆/镍焊接接头强度和韧性方面具有价值，也为相似的异种金属焊接提供参考。

关键词：电子束焊接；复合结构；强韧性协同；力学性能

(Edited by Bing YANG)